

The Preparation of Porous Materials Using Liquid Metal Impregnation for BSE Characterization with a Scanning Electron Microscope

James H. Steele Jr., Consultant
7412 Singing Hills Court, Boulder, CO 80301
james.steele@att.net

Introduction

The infiltration of porous and particulate materials for metallographic examination with low-melting alloys was first described by Rose and DeRoos [1]. The use of Wood's metal to fill porosity in sandstone was reported by Craze [2], by Dullien [3], and by Yadev et al. [4]. Changes in pore structure and phase dispersions in iron ore pellets after simulated blast furnace reduction were reported by Shultz et al. [5], wherein liquid Bi-Sn impregnation was used to prepare cross sections of deformed and reduced pellets for backscatter electron imaging. Steele and Engel [6] also applied the technique to examine the microstructure in commercial boron nitride (BN). In that study porosity formed by leaching the B_2O_3 phase was filled with liquid metal to allow argon-ion etching to expose the BN microstructure. The characterization of cracks and porosity in cement-based materials after filling with Wood's metal has been reported by Nemati et al. [7, 8]. Cracks developed during compression testing of marble were studied by *in-situ* metal impregnation in Chang et al. [9].

The technique, which will be described in this article, involves pressure impregnation with low-melting liquid bismuth (Bi) alloys that shrink or have a low-volume expansion when they solidify. This leads to penetration of open pores according to the classic mercury intrusion relation when the liquid alloy is non-wetting for the material being impregnated (Ritter and Drake) [10]. The diameter of the smallest pore opening penetrated by the liquid metal is given by:

$$d = -4\sigma \cos(\theta) / p \quad (1)$$

In this equation, p is the pressure on the liquid, θ is the contact angle between the liquid and solid being impregnated, and σ is the surface tension of the liquid alloy. If the contact angle $\theta \sim 140^\circ$ and the surface tension $\sigma \sim 480$ dynes/cm (as for mercury with a ceramic material), then $d = 213/p$, where d is in μm when p is in psi. Thus at $p = 5,000$ psi the smallest pore that would be penetrated by the liquid metal would be, $d = 0.04 \mu\text{m}$ (400 Å), and at $p = 10,000$ psi then $d = 0.02 \mu\text{m}$. Hence porous materials and powders with extremely small open porosity can be filled by pressure impregnation with a low-melting liquid alloy and prepared for examination by standard grinding and polishing methods. This infiltration technique is essentially the same as a Mercury Porosimetry experiment of Ritter and Drake [10] with a slightly higher temperature.

Some of the advantages obtained using this mounting technique include grinding and polishing of friable materials without pull-outs or damage to the porous material, char-

acterization using electron probe instruments of many materials without coating, and the ability to argon-ion etch the mechanically polished samples. These advantages will be illustrated by several specific examples of porous materials that are difficult to prepare and examine with an SEM or microprobe.

The Pressure Impregnation Technique

Several commercial alloys that can be used for the impregnation of porous samples and powders are listed with their properties in Appendix 1. These alloys include Bi as the major alloying element, because it produces low-melting eutectic type alloys, and has the unusual property of expanding upon solidification. The most effective alloy, because of its hardness and solidification properties, is *Cerrotru*[™] (58wt%Bi and 42wt%Sn), which solidifies at or below the eutectic temperature of 138°C. Lower melting point alloys, including *CerroBend*[™], which has its eutectic melting temperature at $\sim 70^\circ\text{C}$, and *Indalloy*[™], which melts at $\sim 47^\circ\text{C}$, can be used if the porous material is sensitive to or changed by the 150°C heating required for *Cerrotru*[™].

The pressure impregnation experiment can be carried out in a standard mounting press if O-rings are used for containment of the liquid alloy under pressure. Two O-ring holders must be machined to allow an O-ring seal against both the top and bottom pistons of the mounting press when pressure is applied. Figure 1 shows a schematic diagram of this type of pressure chamber.

Heating the mounting cylinder to above the liquidus temperature for the alloy being used and then increasing the pressure will cause the non-wetting liquid metal to penetrate all open-pore throats larger than diameter d , (as given by the Washburn equation 1). Thus by applying 10 ksi pressure, all open-pore throats larger than about 20 μm (200 Å) will be penetrated and open porosity will be filled with the liquid metal. Cooling the cylinder to solidify the liquid metal while maintaining the pressure will produce a metallographic mount that can be ground and polished by standard methods. Figure 2 shows a macro-photograph of a 1-inch diameter *Cerrotru*[™] mount of a sample of a partially

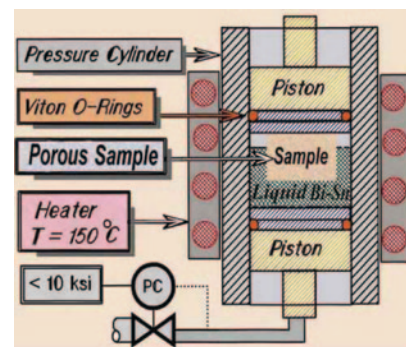


Figure 1: Diagram showing the mounting press with O-rings hold the liquid metal under the pressure needed to infiltrate a porous sample.

Expand your Knowledge of Microscopy with MSA Membership!

Whether your primary focus is in light, electron, or scanning probe microscopy, or the biological or the physical sciences, MSA takes your knowledge to the next level!

Members Receive:

- A personal subscription to MSA's official journal, *Microscopy and Microanalysis*, and MSA's popular bi-monthly magazine, *Microscopy Today*.
- Peer Networking through the Society's Focused Interest Groups and Local Affiliated Societies.
- Discounts on books, journals and other educational materials.
- MSA Awards Programs, Scholarships, Speaker Opportunities, and more!



Join MSA Today!

Visit: www.microscopy.org or call 1-800-538-3672

Solutions for

Titan™ Ultimate



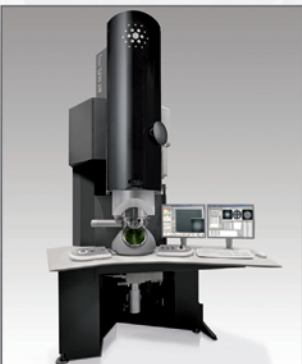
“50 pm resolution, 1 pm precision... we are at the bottom!”

Coming soon...



“I can see *in situ* chemistry down to the atoms.”

Titan™ G2 60-300



“Superior spatial and analytical resolution across the widest, high tension range.”

Coming soon...



“Breakthrough analytics and sub-Ångström imaging from the same instrument.”

Tecnai Osiris™



“Chemical mapping at blazing speeds - my users love this microscope!”

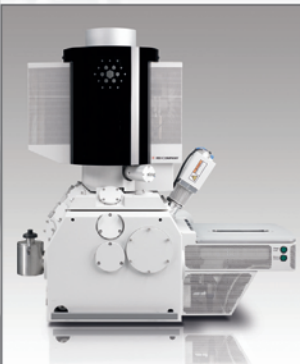
Tecnai™ G2 series



“Delivering on any task, the best workhorse tool we’ve ever had.”

Applied Research

Magellan™ XHR SEM



"I have never seen these details. They're well below the nanometer!"

Helios NanoLab™

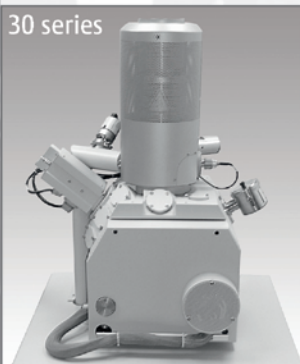
50 series



"Best sample preparation, nanostructuring and SEM to date."

Nova™ NanoSEM

30 series



"My ideal workhorse for nanoscale characterization and analysis."

Quanta™ 3D FEG



"My one-stop shop to prepare and analyze any material, even quartz!"

Quanta™

50 series



"We now produce high quality images and analysis from anything!"

What's next...?

Visit us at M&M,
booth 1048
(August 1-5, 2010)

Visit us at IMC,
booth 50
(September 19-24, 2010)

See beyond at FEI.com/research



Figure 2: Photograph of a 1-inch diameter Cerrotru alloy mount of a partially reduced Taconite (Hematite) pellet from Shultz et al. [5].

reduced hematite pellet as described in Shultz et al. [5].

Results

In the following examples, SEM micrographs of porous materials and powder samples that have been mounted using the pressure-impregnation technique will be presented and discussed. These include images of the following microstructures:

(1) mono-size (0.5 micron) silica sphere packing, (2) New Mexican ancient pueblo pottery, (3) magnesia refractory brick, and (4) wood (dried cedar).

Example 1: Micrographs from a 0.5 Micron Mono-size Silica Sphere Packing

Mono-size silica sphere packings with diameters of 0.2 to 0.5 microns are similar in structure to natural or synthetic opals [11]. Figure 3 shows a secondary electron image from a fracture surface of 425-nm diameter spheres packed in a regular array [12], which shows both $\langle 100 \rangle$ and $\langle 111 \rangle$ type planes. Figures 4 and 5 show backscattered electron images of cross sections

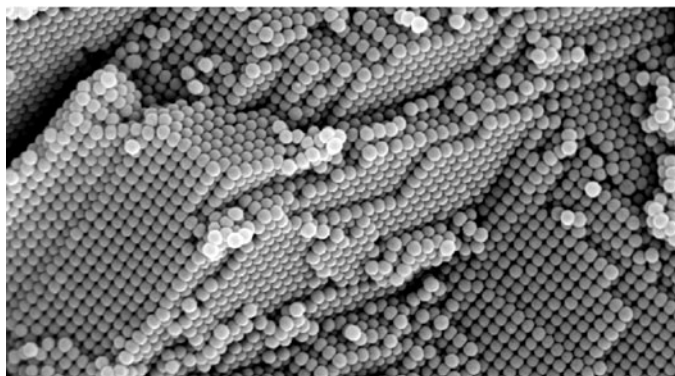


Figure 3: Fracture surface of 425-nm mono-size silica sphere packing showing $\langle 100 \rangle$ type planes and close-packed $\langle 111 \rangle$ -type planes (from Mayoral et al. [12]).

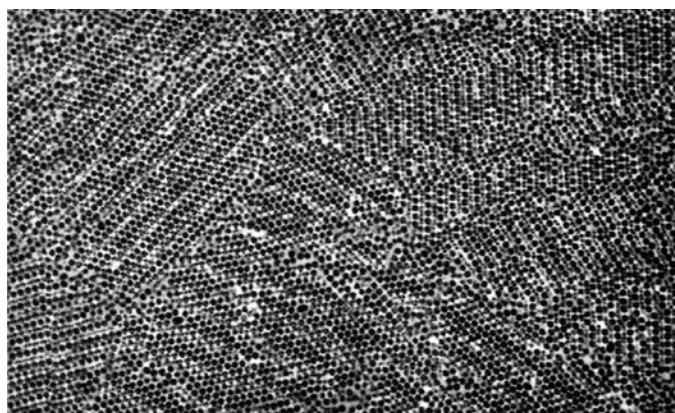


Figure 4: Backscatter image of 0.5 micron silica sphere packing that has been filled with Bi-Sn alloy. The stacking faults and the grain-like packing of the spherical particles can be observed.

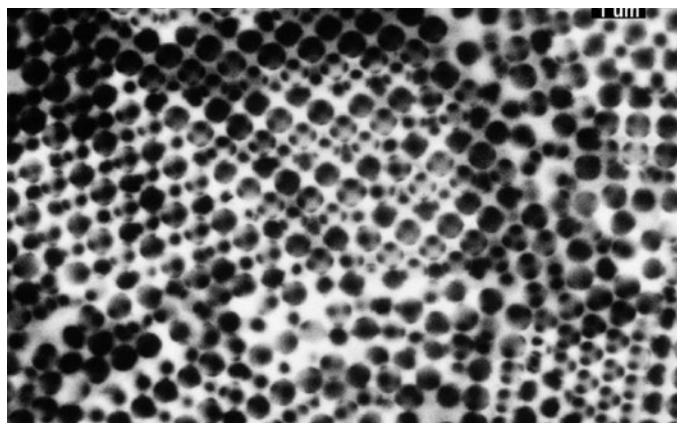


Figure 5: A higher magnification BSE image of a polished section of 0.5 micron silica sphere packing showing filled interstices through the silica particles.

prepared after liquid metal impregnation of a lightly sintered packing of 0.5- μm diameter mono-size silica spheres.

Example 2: Microstructure of Ancient Pueblo Pottery

The microstructure of pottery shards from an Anazazi pueblo ruin in New Mexico [13] were examined after filling with liquid *Cerrotru*[™] and mechanically polishing. The sections were examined using backscatter imaging in an SEM. Figures 6 and 7 are inverted backscatter images that show prior porosity (now filled with Bi-Sn alloy) as dark contrast and clay and temper particles with lighter contrast. The micrographs were obtained without coating. Figure 7 shows the clay microstructure, which has been suggested to be partially transformed to mullite.

Example 3: Magnesia-Chromite Refractory Brick

The microstructure of magnesia (MgO)-chromite (Cr_2O_3) refractory brick [14] is illustrated with the inverted backscatter electron micrographs (shown in Figures 8, 9, 10, and 11). Open porosity is filled with liquid Bi-Sn allowing argon-ion etching to be used to expose fine spinel precipitates within the MgO. These spinel precipitates form as a result of diffusion of Cr or Fe from the chromite or hematite ore particles (Ostyn) [15] where

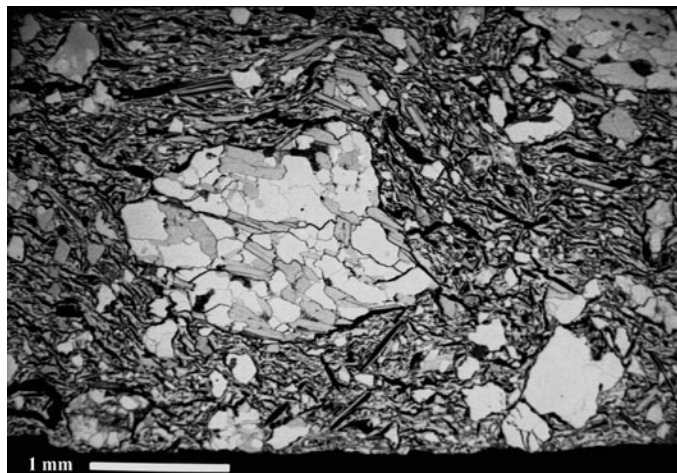


Figure 6: Inverted BS image of pottery shard after filling with Bi-Sn and polishing. Varying gray shades are the result of atomic number contrast.



Figure 7: Higher magnification view of the microstructure of a pottery shard. Note that the clay microstructure consists of two phases that may be the result of incomplete transformation to mullite.

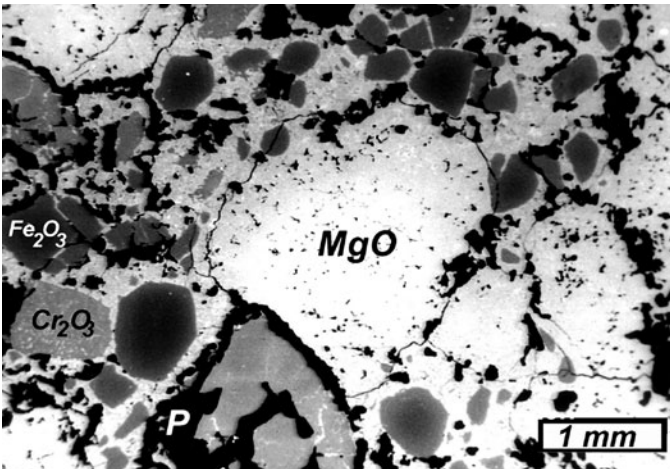


Figure 8: Low-magnification inverted backscatter image of a magnesia-chromite refractory brick. Note: **MgO** = white, Pores (**P**) = black, **Cr₂O₃** = light gray, and **Fe₂O₃** = dark gray.

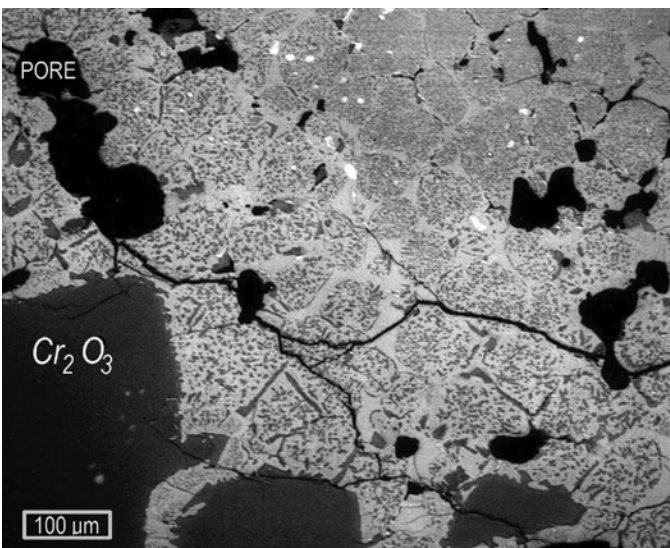


Figure 9: Inverted backscatter image showing chromite interface and spinel precipitates within the MgO phase. The filled pores and cracks that connect them can be readily observed. The scale marker is 0.1 mm.

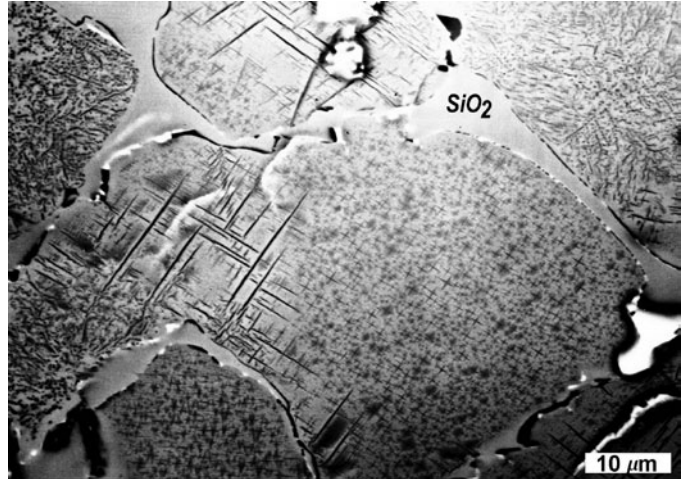


Figure 10: Higher-magnification backscatter image of MgO regions showing **SiO₂** layers separating MgO grains that have fine spinel precipitates formed within them.

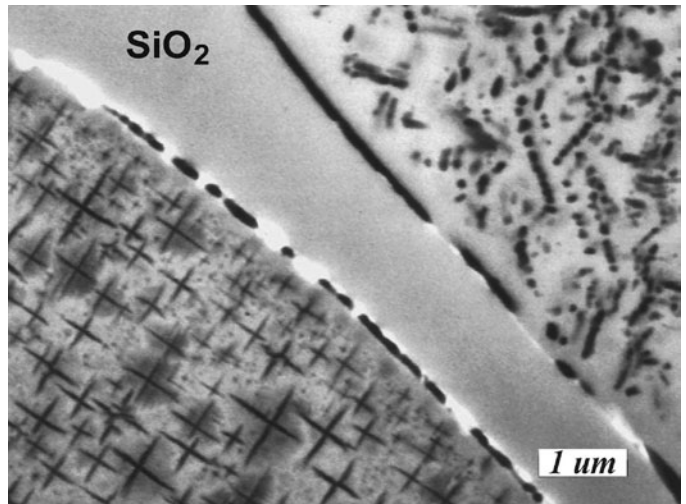


Figure 11: High-magnification inverted backscatter image showing a silica layer between MgO grains that contain fine spinel precipitates. Argon-ion etching of the mechanically polished surface is required to observe these fine cruciform-shaped spinel precipitates.

they are bonded to the MgO. Figure 8 gives a low-magnification inverted backscatter image of the MgO refractory brick, where the Bi-Sn filled pores and cracks are black and the MgO is white. Chromite and hematite ore particles, which are used as initial constituents in the brick, are shown by atomic number contrast with varying shades of gray.

Example 4: Microstructure of Dried Cedar

Figures 12 and 13 show the microstructure of dried cedar in inverted backscatter images. The dark regions are pores that were filled in by the Bi-Sn impregnation. The low-magnification image shown in Figure 12 shows the ring pattern and the different types of cells formed by the tree. The higher-magnification image (Figure 13) shows the fine micro-cracks present in the dried wood and the different types of cells present in cedar. The larger cells are likely vessels, and the double cells separated by a thin wall are likely tracheids (illustrated in Figure 13) in the cedar structure. The cracking pattern in the walls of the fine wood fibers is clearly shown. This cracking

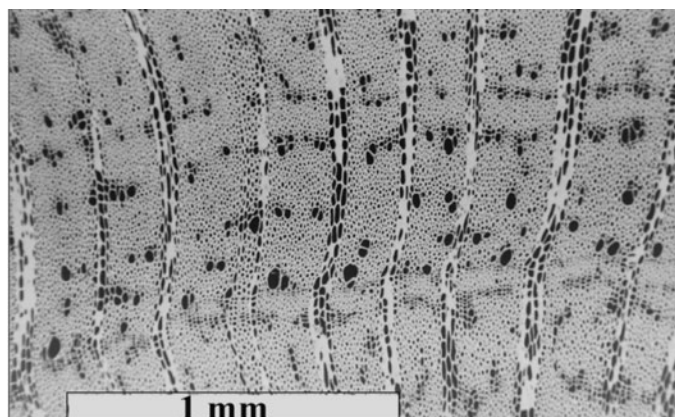


Figure 12: Low-magnification inverted backscatter image of dried cedar. Note the growth rings and the presence of many larger vessels or tracheids.

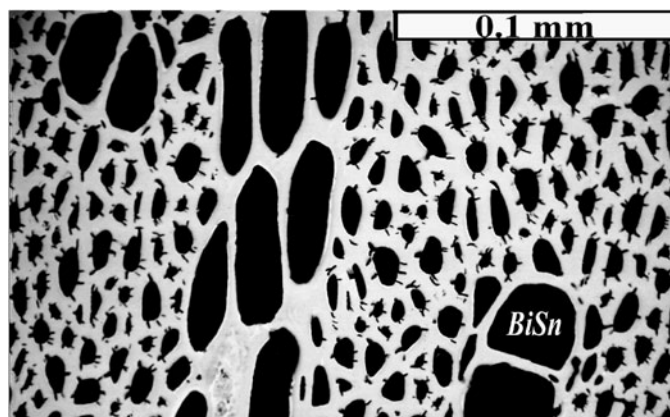


Figure 13: Higher-magnification inverted backscatter image of the microstructure of dried cedar.

Appendix 1: Properties of Low-melting Bi-Sn Alloys from Alloy Digest by Engineering Alloys Digest, Inc. [16]

Property	Cerrotru™	Cerrobend™	Indalloy™
Composition (wt%)	Bi-58% Sn-42%	Bi-50% Pb-27% Sn-13% Cd-10%	Bi-45% Pb-23% In-19% Sn-8% Cd-5%
Density @ 20°C (gm/cc)	8.7	9.4	8.9
Melting Temperature	281°F (138°C)	158°F (70°C)	117°F (47°C)
Volume Change (Liq.-Solid)	+0.77%	-1.7%	-1.4%
Tensile Strength	8,000 psi	5,990 psi	5,400 psi
Brinell Hardness	22	9.2	12

- [13] J Steele, *Micros Microanal* 15 (supp 2) 2009, paper 474.
 [14] JH Steele, *Micros Microanal* 8 (supp 2) 2002, p. 1262CD.
 [15] KM Ostyn, CB Carter, M Koehne, H Falke, and H Schmalzried, *J Am Ceram Soc* 67(10) (1984) 679–685.
 [16] Engineering Alloys Digest, Inc., *Alloy Digest*, Upper Montclair, NJ, 1975.

may be the result of drying or some type of decay in the cedar, as the sample was a piece of a dead branch.

References

- [1] ET Rose and LF DeRoos, “Infiltration of Metallographic Specimens with Metallic Alloys” in *Microstructural Science*, Volume 1, RJ Gray and JL McCall (eds.), Elsevier, New York, 1974, pp. 275–281.
 [2] RC Craze, *Pet Trans*, AIME 189 (1950) 287–293.
 [3] FAL Dullien, *Powder Technol* 29 (1981) 109–116.
 [4] GD Yadev, FAL Dullian, I Chatzis, and IF Macdonald, “Microscopic Distribution of wetting and Non-Wetting Phases in Sandstone During Immiscible Displacements,” paper 13212 in *Proc SPE Annual Technical Conf*, Dallas, (1984).
 [5] RL Shultz, RG Lyons, and JH Steele, *Trans I&SM* (1986) 45–54.
 [6] JH Steele and R Engel, *Adv Ceram Mater* 3 (1988) 452–456.
 [7] KM Nemati, PJM Monteiro, and KL Scrivener, *Am Concrete Inst Mat J* 95 (1998) 617–631.
 [8] KL Scrivener and KM Nemati, *Cement Concrete Res* 26 (1996) 35–40.
 [9] CT Chang, PJM Monteiro, KM Nemati, and K Shyu, *J Mater Civil Eng* 8 (1996) 157–170.
 [10] HL Ritter and LC Drake, *Ind & Eng Chem Anal Ed* 17 (1945) 782–791.
 [11] Y Xia, B Gates, Y Yin, and Y Lu, *Adv Mater* 12 (2000) 693–713.
 [12] R Mayoral, J Requena, C Lopez, SJ Moya, H Miguez, L Vazquez, F Meseguer, M Holgado, A Cintas, and A Blanco, *Adv Mater* 9 (1997) 257–260.

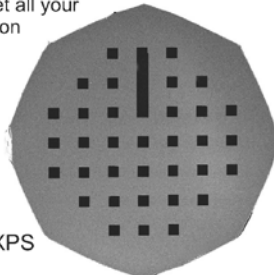
SMART Grids™
Functionalized substrates for advanced analysis

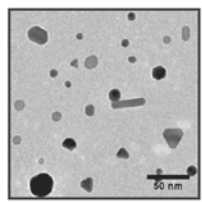
SMART Grids simplify characterization by changing the rules of sample preparation.

Our new NanoGrids™ and BioGrids™ provide application-specific solutions to meet all your sample preparation needs for electron microscopy.

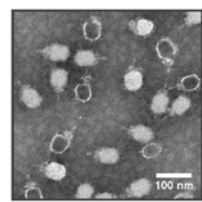
SMART Grids:

- ☑ Reduce artifacts
- ☑ Reduce sample prep time
- ☑ Improve reproducibility
- ☑ Simplify data interpretation
- ☑ Allow for direct correlative analysis: SEM, TEM, AFM, XPS





Gold nanoparticles on NanoGrids



Bacteriophage on BioGrids

For more information or to order SMART Grids, visit:
www.dunesciences.com
 or contact us directly at:
smartgrids@dunesciences.com
 Phone: +1-541-359-4710